공학석사 학위논문

Well-aligned Fe-incorporated Ni-Mo-P nanoarray for highly efficient overall water splitting in alkaline media

알칼리 수전해를 위한 Fe가 함유된 Ni-Mo-P 나노 어레이 촉매의 제조

2019년 8월

서울대학교 융합과학기술대학원

융합과학부 나노융합전공

김 대 규

Well-aligned Fe-incorporated Ni-Mo-P nanoarray for highly efficient overall water splitting in alkaline media

지도 교수 박 원 철

이 논문을 공학석사 학위논문으로 제출함

2019년 6월

서울대학교 융합과학기술대학원

융합과학부 나노융합전공

김 대 규

김대규의 공학석사 학위논문을 인준함

2019년 7월

위 원 장 _____ (인)

부위원장 _____ (인)

위 원 _____ (인

Well-aligned Fe-incorporated Ni-Mo-P nanoarray for highly efficient overall water splitting in alkaline media

Daekyu Kim

Program in Nano Science and Technology

Graduate School of Convergence Science & Technology

Seoul National University

Abstract

The production of hydrogen and oxygen via electrolysis is being recognized as a rising technology to handle the future energy crisis. Thus, fabricating highly active and cost-effective electrocatalysts toward HER and OER is essential to improve the water splitting efficiency. Herein, the Fe-incorporated Ni-Mo-P array on nickel foam (denoted NMFP) was synthesized and used as electrocatalyst for overall water splitting in alkaline media. The preparation of NMFP begins with a hydrothermal treatment of NiMoO4·xH2O nanoarray on nickel foam (denoted as NMO), followed by the modification of Prussian blue analogue (PBA). After the subsequent phosphorization process, the NMFP is successfully synthesized. In the synthesis procedure, $NiMoO_4 \cdot xH_2O$ serves as a sacrificial template and $K_3[Fe(CN)_6]$ acts as Fe sources as well as an organic linker for growth of Ni-Fe PBA on it. As a result, NMFP exhibits remarkable catalytic activity and long term performance in both HER and OER in 1.0 M KOH. In addition, overall water splitting cell with using NMFP as both the cathode and anode has small operating voltage and long-term operation with little loss of activity in 1.0 M KOH. This research can broaden an insight into the fabrication of polymetallic compounds with well-organized to further improve water electrolysis. Furthermore, the proposed synthesis method can be extended to a variety of energy storage and conversion applications.

Keywords: Overall water splitting, Nickel molybdate, Templated synthesis, Metal phosphate

Student Number: 2017-20540

Contents

1. Introduction 13

1.1. Electrochemical water splitting in alkaline media 13

1.2. TMPC for overall water splitting 14

1.3. Fabrication strategies for efficient electrocatalysts 15

1.4. The purpose of our research 16

2. Experimental 17

2.1. Reagents 17

2.2. Preparation of NMO 17

2.3. Preparation of NMF 18

2.4. Preparation of NMFP and NMOP 18

2.5. Material characterizations 19

2.6. Electrochemical measurements 20

3. Result and Discussion 21

3.1. Material analysis 21

3.2. Electrochemical analysis 38

4. Conclusion 59

References.....60

국문 초록 (Abstract in Korean) 75

List of Figures

Figure 1. Schematic illustration of the synthesis procedure of NMFP. ...23

Figure 2. Optical photographs of the prepared catalysts. Nickel foam (a), NMO (b). NMO after reacted with $K_3[Fe(CN)_6]$ for 1 h (C), 3 h (d), 5h (e), and NMFP (f). 23

Figure 3. SEM images of NMO (a, b), NMF (c, d), and NMFP (e, f). ...26

Figure 4. SEM image of NMO after reacted with $K_3[Fe(CN)_6]$ for 1 h (a), 5 h (b). 27

Figure 5. SEM images of NMO after reacted with $K_3[Fe(CN)_6]$ for 24 h. 27

Figure 6. TEM images (a, b) and HR-TEM images (c-e) of NMFP. 29

Figure 7. STEM image of NMFP (a) and the corresponding elemental

mapping image of Ni (b), Fe (c), Mo (d), P (e), and O (f).....30

Figure 8. EDS spectrum of NMFP. 31

Figure 9. Summarized XRD patterns of the prepared materials (a). The characteristic XRD pattern of NMO (b), of NMF (c), and NMF (d). 33

Figure 10. XPS spectra of NMFP. The survey spectrum (a) and the high-resolution spectrum of Ni 2p (b), Mo 3d (c), Fe 2p (d), P 2p (e), and O 1s (f). 35

Figure 11. BET analysis of NMO, NMF, and NMFP. N_2-adsorption-desorption isotherm (a) and the corresponding pore distribution diagram (b). 37

Figure 12. HER and OER LSV curves without iR-compensation of the prepared catalysts according to various reaction time with $K_3[Fe(CN)_6]$. 39

Figure 13. HER performance of NMFP and compared catalysts in 1.0 M KOH. LSV curves at room temperature (a) and the corresponding Tafel slopes (b). Summary of overpotential at current density of 10 $mA \cdot cm^{-2}$ and Tafel slope of the prepared catalysts (c). Time-dependent current density curve of NMFP at fixed overpotential of 15 mV (d). 42

Figure 14. OER characteristics of the prepared catalysts in 1.0 M KOH. LSV curves at room temperature (a) and the corresponding Tafel slopes (b). Summary of overpotential at current density of 10 $mA \cdot cm^{-2}$ and Tafel slope of the prepared catalysts (c). Time-dependent current density curve of NMFP at fixed overpotential of 240 mV (d). 46

Figure 15. EIS spectra of the prepared catalysts for HER (a) and OER (b) in 1.0 M KOH. 49

Figure 16. Randles circuit used for modeling of HER and OER kinetic processes. 49

Figure 17. CV curves of NMO (a), NMOP (b), NMF (c), and NMFP (d) in 1.0 M KOH with different scan rates. Linear plots of differences in current density of NMO, NMOP, NMF, and NMFP as a function of scan rate (e). 52

Figure 18. Overall water splitting performance of NMFP || NMFP in 1.0 M KOH. Comparison of polarization curves between NMFP || NMFP and Pt/C || RuO_2 (a). Polarization curves of NMFP || NMFP before and after 3000 cycles (b). Long-term stability test of NMFP || NMFP to maintain 10 $mA \cdot cm^{-2}$ for 40 h (c). Photograph image of NMFP || NMFP water electrolyzer (d). ..55

Figure 19. SEM images of NMFP after electrolysis for 40 h. NMFP at the cathode (a, b), NMFP at the anode (c, d). 57

Figure 20. XPS analysis of NMFP at the anode after electrolysis. Ni 2p (a), P 2p (b), O 1s (c), Fe 2p (d), and Mo 3d (e). 58

List of Tables

Table 1. BET surface area, pore volume and mean pore diameter of NMO, NMF, and NMFP. 37

Table 2. Summary of HER and OER performance of NMFP- 1h, NMFP, and NMFP- 5h. 39

Table 3. Comparison of the HER performance of NMFP with other reported electrocatalysts in 1.0 M KOH. 43

Table 4. Comparison of the OER performance of NMFP with other reported electrocatalysts in 1.0 M KOH. 47

Table 5. Summary of each circuit parameters under the HER process. .50

Table 6. Summary of each circuit parameters under the OER process. 50

Table 7. Summary of the calculated C_{dl} of NMFP and compared

materials. 53

1. Introduction

1.1. Electrochemical water splitting in alkaline media

Electrochemical water splitting for hydrogen (H_2) and oxygen (O_2) generation has been considered as a promising technology to provide clean and sustainable energy platforms to handle the future energy crisis and environmental pollution [1-3]. Furthermore, to satisfy the imminent demand of applications for energy conversion such as fuel cells (FCs), better technology for water electrolysis is needed [4,5]. Especially, in order to avoid the contamination of the electrolytic cell and produced gas, it is better for the reaction to take place under alkaline medium [6]. However, because of the reaction mechanism, the hydrogen evolution reaction (HER) under alkaline electrolyte requires additional energy to overcome the activation overpotential and considered an inefficient process. Also, the overall water splitting efficiency is always adversely affected by sluggish kinetics of oxygen evolution reaction (OER). These critical drawbacks leading to the insufficient gas production at the anode the cathode of overall water splitting cells [7-9]. Therefore, efficient electrocatalysts are required to reduce the energy input and accelerate the water electrolysis to achieve the goal of massive industrial applications in the near future.

Conventionally, the commercial electrolyzer uses Pt, Ru and Ir based catalysts, which are known as the noble metals [10,11]. However, a huge economic drawback, mediocre durability, and insufficient amount of these precious materials prohibit them from large-scale applications [12-14]. Furthermore, incorporating different catalysts for the anode and the cathode of a water electrolytic cell requires a complicated process and additional costs [15,16]. Therefore, it is highly desirable to design a cost-effective and competent catalyst for both HER and OER in the same media based on earth-abundant elements.

1.2. TMPC for overall water splitting

The past studies have demonstrated that transition metal phosphorous composites (TMPC) are adequate electrocatalysts for overall water splitting [17-20]. It has been reported that this intriguing functionality of TMPC results from optimal metal-hydrogen bonding energy for HER and low energy barrier for OER active species. [21-24]. Among the possible precursor materials for the highly efficient TMPC, Ni-Mo derivatives have received attention in recent years [25-29]. From the computational and experimental studies, their exceptional HER activity is due to the fast water dissociation attributed

to Ni and optimized adsorption properties of Mo [30,31]. However, despite much progress, further research is required to produce ideally designed and high efficient electrocatalysts to reach the practical application.

1.3. Fabrication strategies for efficient electrocatalysts

In order to develop a well-designed and highly active catalyst, one of the nominated strategies is to prepare an architecture of well-aligned 1D-structured nanomaterial directly on 3D hierarchical porous conductive substrates. By doing so, the architectural advantage not only provides plenty of exposed active sites but also facilitates the ion diffusion and electron transfer [32,33]. In addition, the structural superiority can promote the gas bubble desorption from the catalyst surface to reduce the ohmic resistance on the electrode surface which can boost the gas evolution efficiency [34]. For example, Li *et al.* [27] synthesized $Ni(PO_3)_2$-MoO_3 nanoarrays directly on nickel foam for overall water splitting catalyst. Also, hybridazation of multi metallic elements is another method to improve the intrinsic activity of catalysts [35-38].

For example, Chen *et al.* [39] proved that Fe doping effectively improved the OER performance by altering the electronic structure of host material and enlarging the electrochemically active surface area. Yuancai *et al.* [40] reported that templated grown Ni-Fe PBA-induced bimetallic phosphide (Ni_2P/Fe_2P) for efficient HER.

1.4. The purpose of our research

Based on the abovementioned perspectives, a vertically-oriented Fe-Ni-Mo-P nanoarray on nickel foam (denoted as NMFP) was made for overall water splitting electrocatalyst in alkaline solution. Initially, $NiMoO_4 \cdot xH_2O$ nanoarray was synthesized directly on Ni foam (denoted as NMO) using the hydrothermal treatment. Subsequently, Fe was successfully integrated in the form of pussian blue analogue (PBA) onto the NMO surface, followed by further alteration via phosphorization. In this method, $NiMoO_4 \cdot xH_2O$ acts as both Ni source and sacrificial template. Because of the architectural advantage of well-oriented nanoarray, the successful confinement of PBA was feasible to maximize the potential active sites. $K_3[Fe(CN)_6]$ plays a role in Fe sources as well as an organic linker for the formation of PBA. Benefiting from the addition of Fe into Ni-Mo-P as well as its well-

ordered structure on nickel foam, as-synthesized NMFP exhibits excellent water splitting capability in alkaline solution. NMFP requires a low overpotential of 15 mV and 240 mV to reach 10 $mA \cdot cm^{-2}$ and has a Tafel slope of 77.65 $mV \cdot dec^{-1}$ and 56.51 $mV \cdot dec^{-1}$ for HER and OER, respectively. Furthermore, its catalytic performance for HER and OER is maintained for 40 h continuous runs. A water electrolyzer based on NMFP electodes requires only 1.63 V to reach the current density of 100 $mA \cdot cm^{-2}$ and shows little activity loss after 3000 cycle runs.

2. Experimental

2.1. Reagents

All chemicals were used without further purification. Sodium molybdate dehydrate ($Na_2MoO_4 \cdot 2H_2O$, 99.5%), potassium ferricyanide ($K_3[Fe(CN)_6]$, 99%) and Nafion solution (5 wt%) were purchased from Sigma-Aldrich (USA). Sodium phosphinate monohydrate ($NaH_2PO_2 \cdot H_2O$, 97.0%) was purchased from Junsei Chemical (Japan). Nickel nitrate hexahydrate ($Ni(NO_3)_2 \cdot 6H_2O$, 98.0%), ethanol (99.9%) and potassium hydroxide (KOH, 99.9%) were purchased from Samchun Chemicals (South Korea).

2.2.1. Preparation of NMO

The $NiMoO_4 \cdot xH_2O$ was directly synthesized on nickel foam by a simple hydrothermal method. Before the hydrothermal process, commercial nickel foam (NF, $1.0 \times 3.0\ cm^2$) was successively cleaned for 15 minutes by 3.0 M HCl, acetone, and ethanol to remove the surface oxide layer. Then, the as-treated NF was immersed into 12 ml of a mixture solution containing $Ni(NO_3)_2 \cdot 6H_2O$ (0.1164 g) and $NaMoO_4 \cdot 2H_2O$ (0.0968 g) in a 20 ml capacity of Teflon line autoclave. For the next step, the Teflon line autoclave is heated in an oven at 160 ℃ for 6 h. Finally, the sample was ultrasonicated in a water bath for a few seconds and rinsed by ethanol and dried in a drying oven at 60 °C overnight. The prepared electrode was denoted as NMO.

2.2.2. Preparation of NMF

First, $K_3[Fe(CN)_6]$ (1.5 mg) was dissolved in 10 ml deionized water. Then, the as-prepared NMO was submerged into the above solution and kept under stirring for 3 hours. Finally, the Ni-Fe PBA-NMO was washed with deionized water and ethanol several times and dried in the drying oven at 60 ℃ overnight. After the preparation, the electrode was denoted as NMF.

2.2.3. Preparation of NMFP and NMOP

A porcelain boat with NMF was placed in the center of a tube furnace, and another porcelain boat with $NaH_2PO_2 \cdot H_2O$ (300 mg) was placed on the upstream side of the tube furnace. Then the tube furnace was heated to 350 ℃ with a heating rate 2 ℃ min^{-1} and kept for 2 h under Ar flow atmosphere. Then, the resultant was washed with deionized water and ethanol several times and dried in the drying oven at 60 ℃ overnight. After the preparation, the electrode was denoted as NMFP. The synthesis procedure of Ni-Mo-P (denoted as NMOP) is the same as the NMFP preparation process without the PBA modification step.

2.3. Materials characterization

X-ray diffraction (XRD) patterns were recorded by a powder X-ray diffractometer (SmartLab, Rigaku, Japan) with a Cu target and a scan rate of 5 ° min^{-1}. Field-emission scanning electron microscope (FE-SEM, Hitachi S-4800, 15 kV) was used to examine the structural morphology of the sample. High-resolution transmission electron microscopy (HRTEM, JEOL JEM-2100F, 200 keV) equipped with the energy-dispersive X-ray spectroscopy (EDS) was also utilized to further structural characterization. The specific surface area and pore volume were analyzed via nitrogen adsorption-

desorption isotherm (Micrometrics ASAP 2010). X-ray photoelectron spectroscopy (XPS) spectra were obtained by using a Sigma probe (ThermoFisher Scientific, U.K) with a moveable Al X-ray source.

2.4. Electrochemical measurements

Electrochemical measurements were performed with an Autolab potentiostat (Metrohm, Netherlands) in a three-electrode setup using 1.0 M KOH solution. The as-prepared catalysts on NF (1.0 cm^2 in area, loading mass ~ 5.2 $mg \cdot cm^{-2}$) were used as a working electrode. Platinum plate (1.0 cm^2 in area) and Hg/HgO (in 1.0 M NaOH solution) were used as a counter and a reference electrode, respectively. To use RuO_2 and Pt/C as the control samples, the catalyst inks were prepared by mixing 4.95 mg of the RuO_2 or Pt/C with a mixture of 0.75 mL of ethanol and 0.20 mL of deionized water, and 0.02 mL of Nafion solution (5 wt%). Then, the prepared ink was loaded on NF with an area of 1.0 cm^2 (the amount of mass loading is the same as those of synthesized catalysts)

All measured potential were converted to the reversible hydrogen electrode (RHE) according to following equation: $E_{RHE} = E_{Hg/HgO} + 0.059 \cdot pH + 0.140$

It should be mentioned that any indication regarding the potentials is referred to RHE in 1.0 M KOH solution without specification. To acquire HER data,

the electrolyte was initially purged with N_2 for 30 min. Before Linear sweep voltammetry (LSV) test, a conditioning step was applied by cyclic voltammetry (CV) for 10 cycles between 0.08 and -0.70 V with a scan rate of 5 $mV \cdot s^{-1}$. LSV was conducted with a scan rate of 1 $mV \cdot s^{-1}$ to measure HER activity. In the case of OER test, the electrolyte was purged with O_2 for 30 min. Prior to LSV test, a conditiosning step was applied by CV for 10 cycles between 0.96 and 1.76 V with a scan rate of 5 $mV \cdot s^{-1}$. Then, LSV was performed with a scan rate of 1 $mV \cdot s^{-1}$ to measure OER activity. To evaluate the long-term performance, chronoamperometry (CA) was conducted at constant overpotentials of 15, 240 mV for HER and OER, respectively. The electrochemical double layer capacitance (C_{dl}) of different catalysts were measured by using cyclic voltammetry in a non-faradaic potential region (0.20 – 0.30 V) at series of scan rates of 20, 40, 60, 80, and 100 $mV \cdot s^{-1}$. The C_{dl} was calculated as follows: $C_{dl} = \Delta j / \upsilon$, where $\Delta j = j_a - j_c$: charging current ($mA \cdot cm^{-2}$) at 0.25 V and υ : scan rate ($mV \cdot s^{-1}$). Electrochemical impedance spectroscopy (EIS, ZIVE SP1) was used to investigate the interfacial charge-transfer resistances of the resultant catalysts. EIS measurements were carried out in the frequency range from 10^{-2} to 10^5 Hz at -0.1 V and 1.60 V for HER and OER respectively. Unless otherwise stated, an 80% iR-compensation was applied to the LSV curves.

3. Result and Discussion

3 .1 Material analysis

The overall synthesis procedure is described in detail in the experimental section and outlined in Figure 1. First, the NMO was prepared with $NiMoO_4 \cdot xH_2O$, which was directly grown on nickel foam by the hydrothermal method. Then, as-prepared NMO was immersed into $K_3[Fe(CN)_6]$ solution for 3 h at room temperature to form NMF. Finally, NMF was treated by the subsequent phosphorization process to produce NMFP. As shown in Figure 2, the surface color of nickel foam was changed into light green, illustrating the formation of NMO. The gradual change in surface color from light green to yellow indicates that PBA was formed on the NMO surface and became NMF. After the phosphorization process, the color of the surface was changed from yellow to black, indicating that the successful production of NMFP.

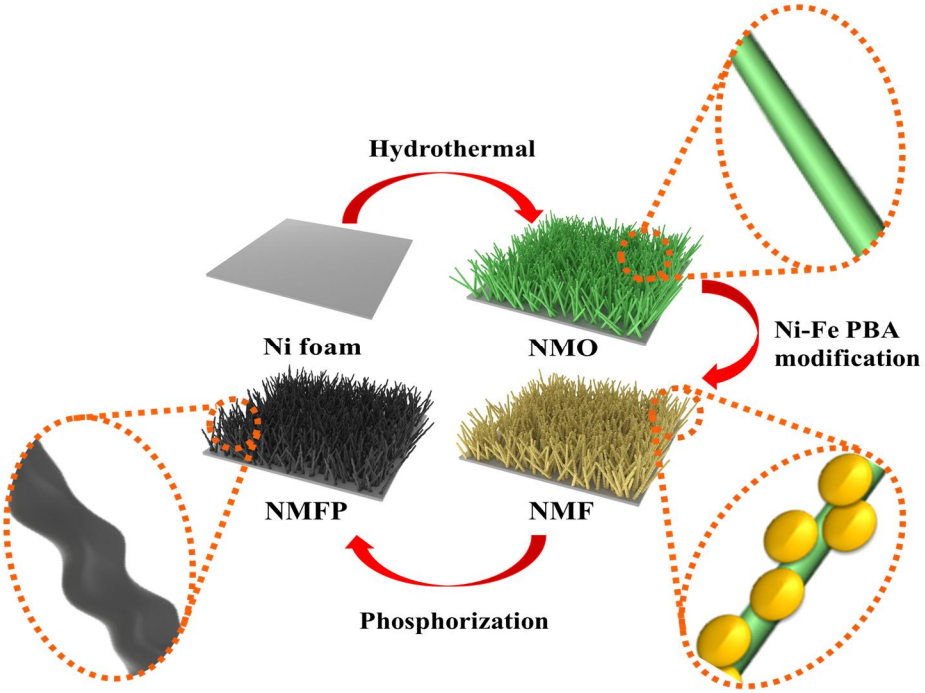

Figure 1. Schematic illustration of the synthesis process of NMFP.

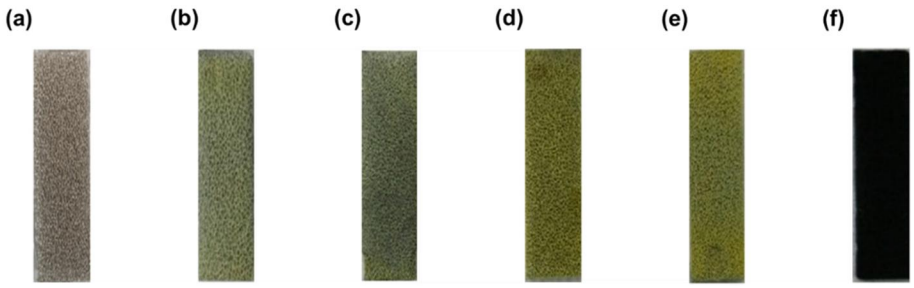

Figure 2. Optical photographs of the prepared catalysts. nickel foam (a), NMO (b). NMO reacted with $K_3[Fe(CN)_6]$ for 1 h (C), 3 h (d), 5h (e), which are denoted as NMF -1h, NMF, and NMFP-5h, respectively. NMFP (f).

The growth process and morphology of materials were initially investigated by SEM analysis. As seen in Figure 3a and b, the as-synthesized NMO showed rod-like morphology with a diameter of ca. 100 nm and length of few microns. Also, the NMO image indicated that the nanorods were vertically-anchored on the nickel foam. After immersing the NMO into $K_3[Fe(CN)_6]$ solution for just 1h, noticeable morphological change was not observed in Figure 4a. When the reaction time reached 3 h, PBA nanoparticles with sizes of ca. 200 nm in width grew uniformly along the surface of NMO nanorod (Figure 3c, d). By this method the PBA nanoparticles were formed in the way of ordered and confined structure. However, the small fraction of nanorod was collapsed after a reaction time of 5 h (Figure 4b) and severely damaged when the reaction time was prolonged to 24 h (Figrue 5). This unique hierarchical structure could be attributed to a two-step chemical etching and co-precipitation method [41,42]. In the process, $K_3[Fe(CN)_6]$ could act as a mild oxidant that would be able to dissolve the metal oxides locally. Furthermore, it is possible that a portion of Ni^{2+} were removed from the NMO and react with $[Fe(CN)_6]^{3-}$ to form Ni-Fe PBA. In the case of NMFP, the nanorod structure was well preserved and still fixed to the nickel foam except for a minor reduction in size. In addition, the hierarchical surface structure of NMF was changed into

the bean pod-like shaped morphology with the metal phosphates layer (Figure 3e, f) due to the structural reorganization by heating treatment [43]. The previous study proposed that the unique rod-like array anchored on the substrate can provide an efficient electron transport pathway as well as a high density of exposed active sites, promoting electrochemical reaction [44].

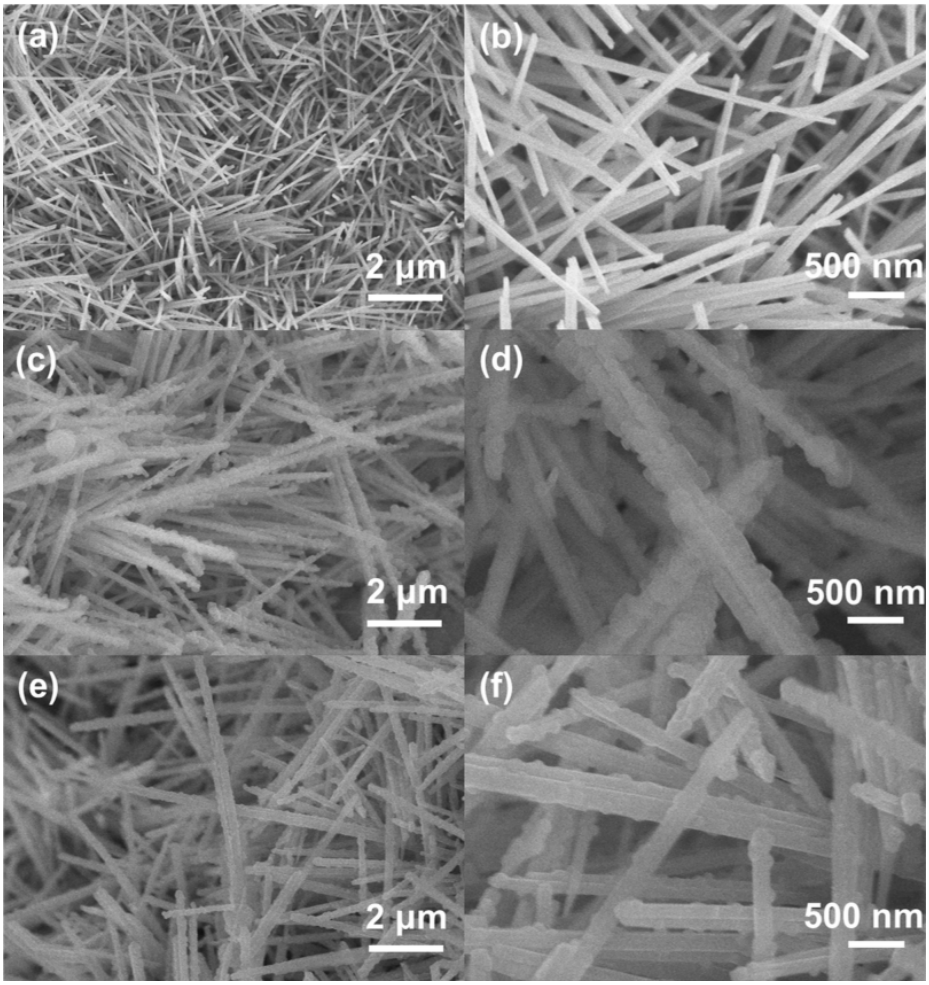

Figure 3. SEM images of NMO (a, b), NMF (c, d), and NMFP (e, f).

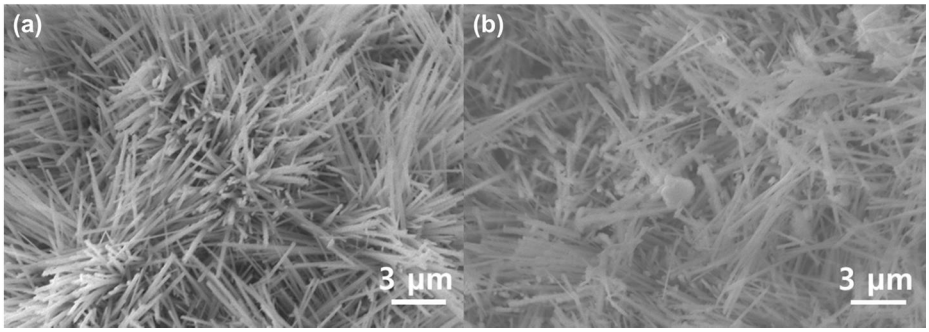

Figure 4. SEM image of NMO reacted with $K_3[Fe(CN)_6]$ for 1 h (a) and 5 h (b).

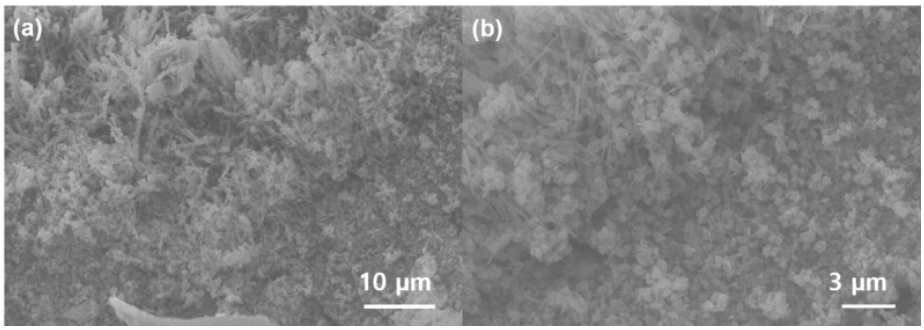

Figure 5. SEM images of NMO reacted with $K_3[Fe(CN)_6]$ for 24 h.

More specific structural features of the NMFP were further elucidated by TEM analysis (Figure 6). The NMFP composite had rod-like structures with the bean-pod resembling surface, which is in good agreement with the SEM images (Figure 6a, b). Moreover, as seen from the HR-TEM image (Figure 6c-e), apparent lattice fringes were not observed. This result means that the NMFP is in amorphous phase which can be beneficial to electrocatalytic reaction due to the abundant unsaturated bonds which serve as extra active sites [17,45]. The spatial distribution of elements in NMFP was determined with EDS mapping (Figure 7) and the EDS spectrum (Figure 8). All the elements (Ni, Fe, P, and O) except Mo were uniformly distributed in the nanorod. The result showed that Mo was mostly distributed in the internal rod of the structure. This result could be explained by the growth mechanism that contains chemical etching and precipitation process, which mentioned above.

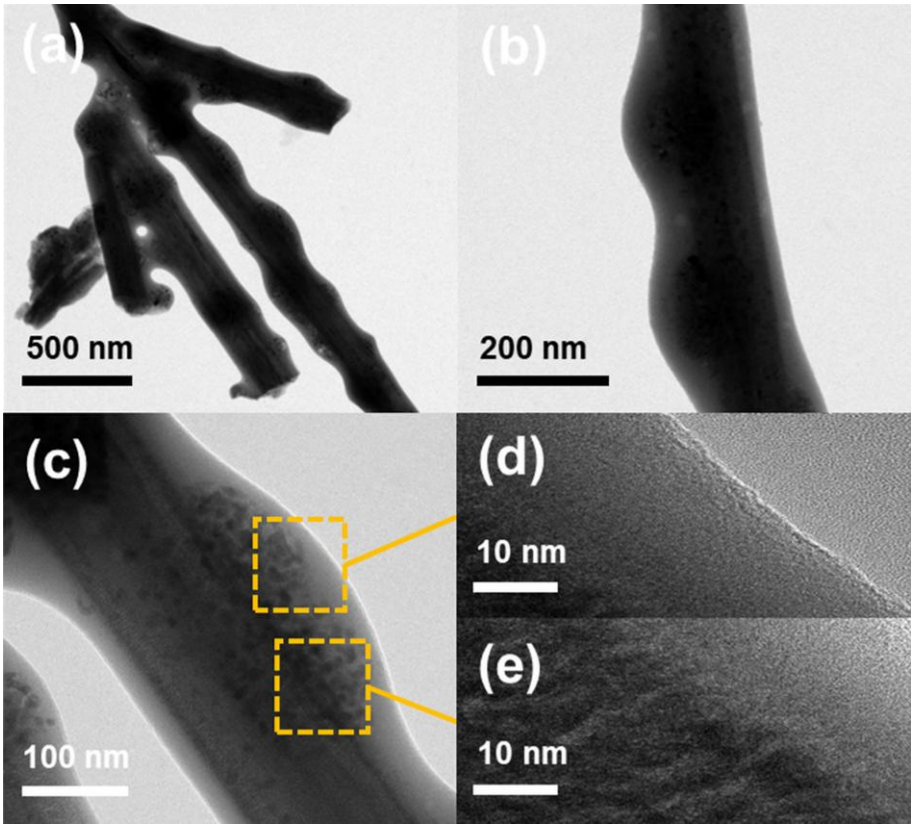

Figure 6. TEM images (a, b) and HR-TEM images (c-e) of NMFP.

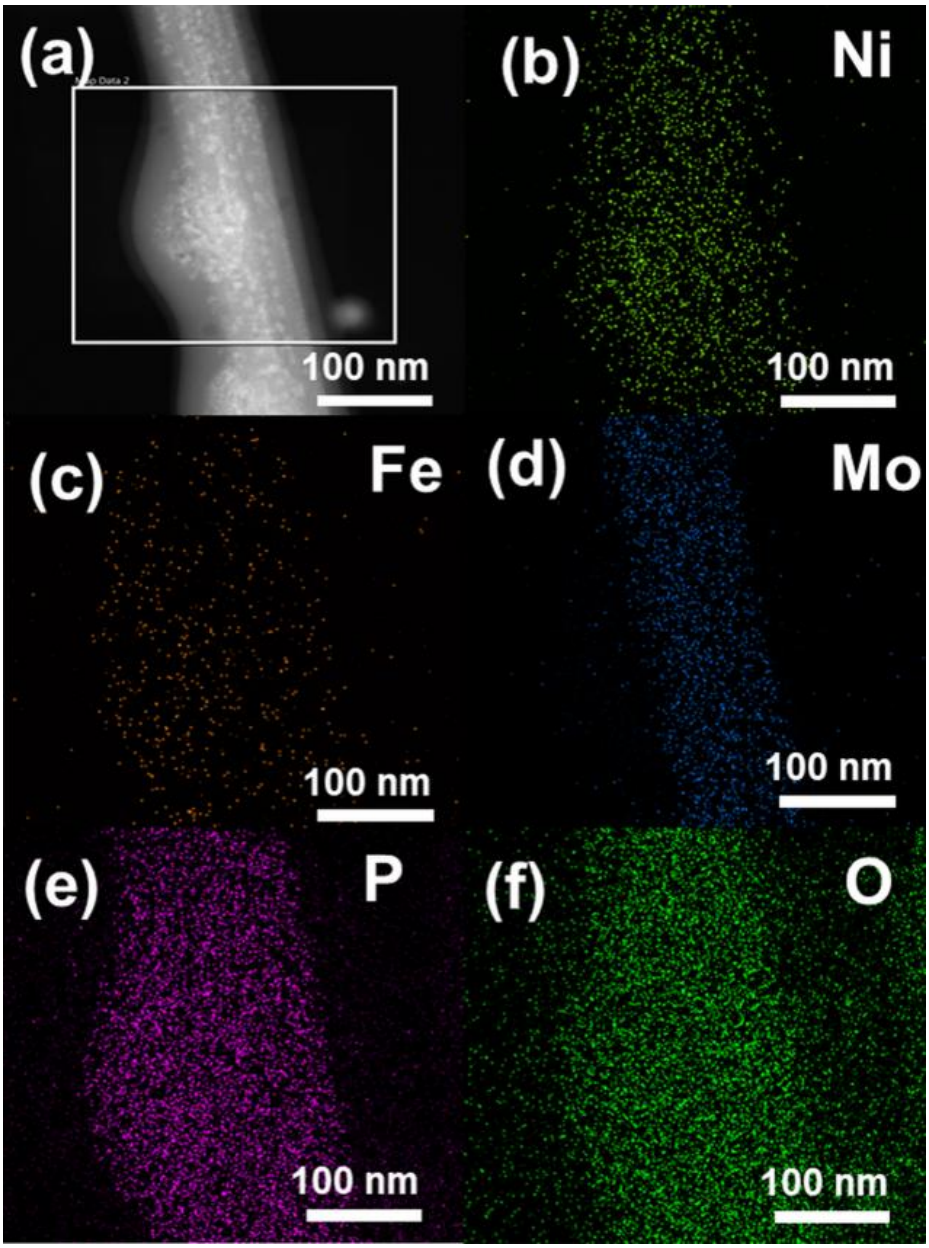

Figure 7. STEM image of NMFP (a) and the corresponding elemental mapping image of Ni (b), Fe (c), Mo (d), P (e), and O (f).

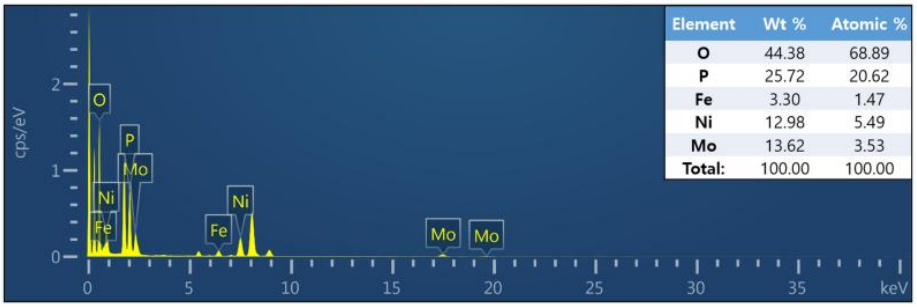

Figure 8. EDS spectrum of NMFP

The crystal structure of the as-synthesized materials was verified by XRD analysis. The overall XRD spectra of the prepared materials are presented in Figure 9a. All the materials showed three distinctive peaks at ~44.5°, 51.8°, and 76.4° were consistent with (110), (200), and (220) crystal planes of Ni metal (JCPDS, No. 65-2865), which can be translated as the characteristics of Ni foam [46]. As seen in Figure 9b, the diffraction patterns of the prepared NMO matched well with those of the reported $NiMoO_4 \cdot H_2O$ (JCPDS, No. 13-0128) [47,48]. However, the detailed crystal planes of $NiMoO_4 \cdot xH_2O$ was unable to observe, which can be explained by the low crystallinity of coordinated water in $NiMoO_4$ [49,50]. As shown in Figure 9c, after reacting with $K_3[Fe(CN)_6]$ for 3 h, the additional peaks at ~14.9°, 17.3°, 24.6°, 35.1°, 39.4°, and 68.6° were observed. These peaks are attributed to (111), (200), (220), (400), (420), and (642) planes of $Ni_3[Fe(CN)_6]_2 \cdot H_2O$ (JCPDS No. 82-2283) [51,52], demonstrating that Ni-Fe PBA was successfully grown on $NiMoO_4 \cdot xH_2O$. The characteristic peaks of NMFP were ambiguous, suggesting that the synthesized NMFP was amorphous (Figure 9d). This consequence well agrees with the HR-TEM results.

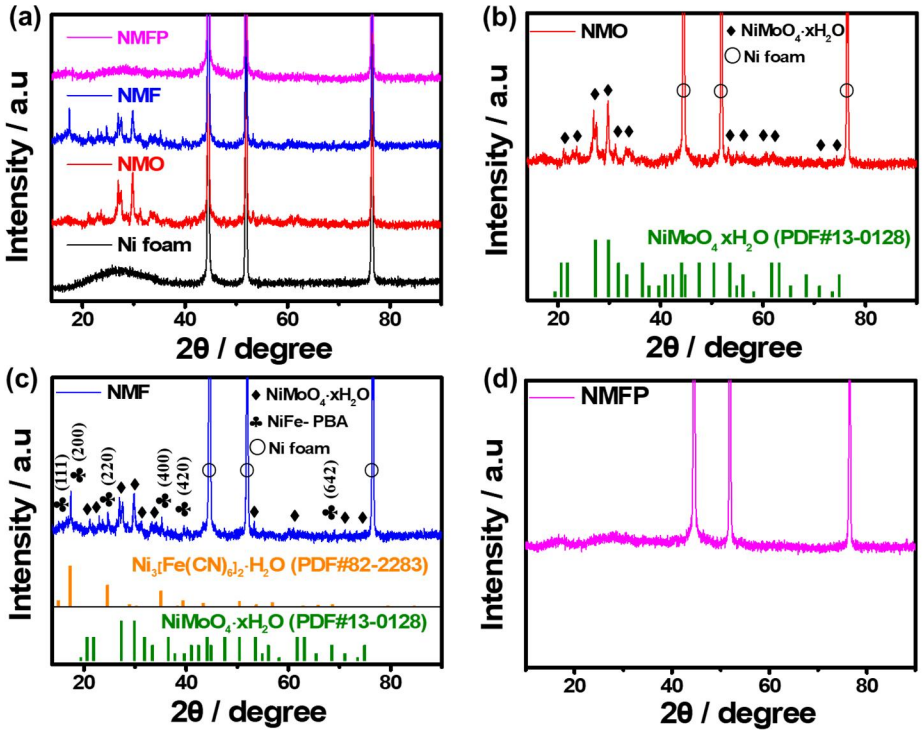

Figure 9. Summarized XRD patterns of the prepared materials (a). the characteristic XRD pattern of NMO (b), NMF (c), and NMF (d).

The chemical valence state of surface elements in NMFP was investigated by XPS. As shown in the overall XPS spectra (Figure 10a), NMFP was composed of Ni, Mo, Fe, P, and O. This agrees well with the EDS mapping results. The high-resolution spectrum of Ni 2p was fitted into 4 contributions (Figure 10b). The main two peaks at 855.9 and 873.9 eV with two satellite peaks at 860.7 and 879.8 eV were attributed to Ni $2p_{3/2}$ and $2p_{1/2}$, respectively. This result indicated the existence of Ni^{2+} state in NMFP [27]. The Mo 3d spectra (Figure 10c) exhibited two distinctive peaks at 232.2 and 235.3eV which were assigned to Mo $3d_{5/2}$ and Mo $3d_{3/2}$, respectively. Furthermore, the interval of the peaks (Δ Mo 3d = 3.1eV) signifed the Mo^{6+} state in MoO_3 [27]. For the Fe 2p spectra (Figure 10d), the binding energy peaks represented at 709.8 and 723.3 eV corresponding to Fe^{2+} $2p_{3/2}$ and Fe^{2+} $2p_{1/2}$. Moreover, the other peaks at 713.1 and 726.7 eV with two satellite peaks at 716.8 and 730.8 eV demonstrated Fe^{3+} $2p_{3/2}$ and Fe^{3+} $2p_{1/2}$, respectively [53]. For the P 2p spectra (Figure 10e), the peaks at 134.4 and 135.4 eV were assigned to PO_3^- and H_3PO_4 species, respectively [27]. This result indicated that the formation of metal phosphate in NMFP [54]. With regard to O 1s (Figure 10f), the peaks at 530.6 and 531.5 eV were indexed to oxygen species in $NiFe_2O_4$ and. M-O (M: Mo and Ni) [55,56]. Other peaks at 532.2 and 533.1 eV were assigned to adsorbed –OH on the NMFP surface

and P-O bond in phosphate, respectively [26,55].

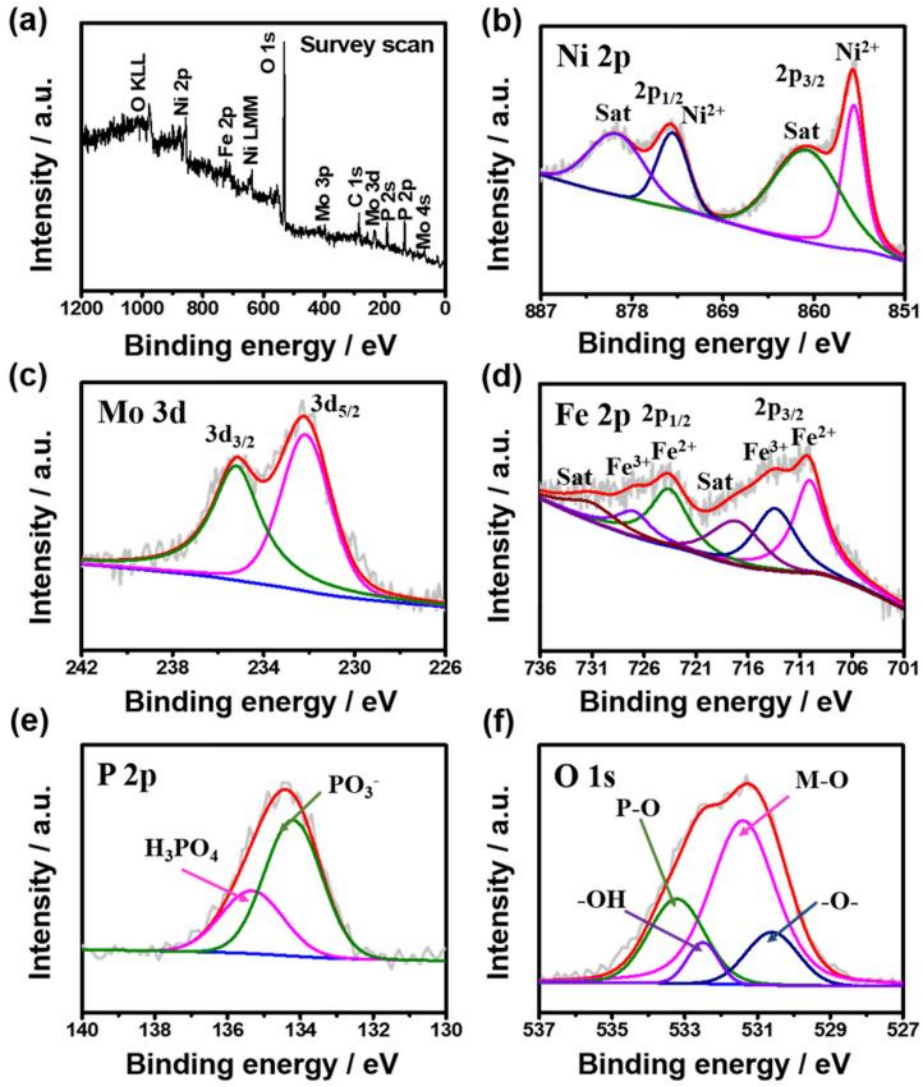

Figure 10. XPS spectra of NMFP. The survey spectrum (a) and the high-resolution spectrum of Ni 2*p* (b), Mo 3*d* (c), Fe 2*p* (d), P 2*p* (e), and O 1*s* (f).

BET surface area, total pore volume and mean pore diameter of the prepared samples were analyzed via nitrogen adsorption-desorption isotherm. All the samples were detached from nickel foam before the test. From N_2 adsorption-desorption plot (Figure 11a), it is plausible to consider that NMO and NMFP possessed the typical type Ⅱ hysteresis, indicating the majority of the existing pores of examined samples are macropores [57]. Judging by the BET plot of NMF, a heavy modification of PBA on NMO results in the increase of mesoporosity, leading to a semi-type Ⅳ hysteresis [58]. This assumption is backed up by the pore diameter distribution plot (Figure 11b), which demonstrates that most of the pores are either mesopores or macropores for the NMO, NMF, and NMFP. A summary of BET analysis is represented in Table 1.

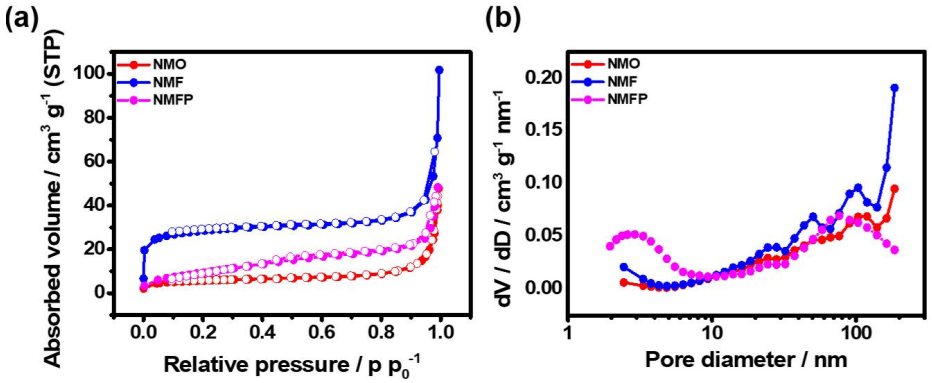

Figure 11. BET analysis of NMO, NMF, and NMFP. N_2-adsorption-desorption isotherm (a) and the corresponding pore distribution diagram (b).

Table 1. BET surface area, pore volume and mean pore diameter of NMO, NMF, and NMFP.

	NMO	NMF	NMFP
BET surface area (m^2 g^{-1})	20.8	104	36.5
Total pore volume (cm^3 g^{-1})	0.06	0.12	0.074
Mean pore diameter (nm)	11.9	4.57	8.17

3.2 Electrochemical analysis

To determine the optimal modification degree of PBA, additional electrochemical data of HER and OER regarding the reaction time (1 – 5 h) with NMO and $K_3[Fe(CN)_6]$ was initiated (Figure 12). The result showed overpotential required to reach 10 $mA \cdot cm^{-2}$ for HER and OER was 23 mV and 250 mV, respectively, for the NMFP, which was the smallest values among the compared sample. From the SEM and LSV for HER and OER results, the reaction time was set to 3 h in order to maximize the catalysis performance. Therefore, unless otherwise mentioned, further investigation into the synthesized materials in this paper is based on NMF with a reaction time of 3 h. Summarized result of electrochemical data is presented in Table 2.

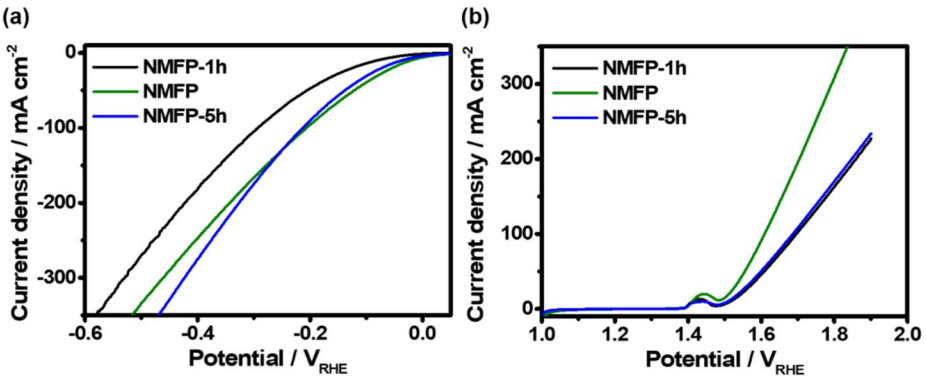

Figure 12. HER and OER LSV curves without iR-compensation of the prepared catalysts according to various reaction time with $K_3[Fe(CN)_6]$.

Table 2. Summary of HER and OER performance of NMFP- 1h, NMFP, and NMFP- 5h

Material	η at 10mA cm^{-2} (mV) for HER	η at 10mA cm^{-2} (mV) for OER
NMFP-1h	81	290
NMFP	23	250
NMFP-5h	37	280

Prior to the use of NMFP as overall water splitting catalyst under alkaline condition, the series of independent electrochemical test of HER and OER was conducted to determine the adequacy of the material as an efficient catalyst. Initially, to find out the effectiveness of NMFP for electrochemical HER catalyst, the investigation was initiated in 1.0 M KOH using a conventional three-electrode system. As obtained LSV curves from the experimented samples (Figure 13a) proved that the synthesized NMFP was the most effective HER catalyst with an overpotential of 15.0 mV to achieve the current density of 10 $mA \cdot cm^{-2}$. The rest of the examined catalysts, for example, NMO (194.0 mV), NMOP (61.0 mV), NMF (174.0 mV), and Ni foam (195 mV) showed insufficient outcomes. For extended investigation toward HER kinetics, the Tafel plot (Figure 13b) was acquired from each LSV curves to estimate the Tafel slope. The prepared NMO (110.1 $mV \cdot dec^{-1}$), NMOP (97.16 $mV \cdot dec^{-1}$), NMF (131.34 $mV \cdot dec^{-1}$) and Ni foam (208.9 $mV \cdot dec^{-1}$) showed stiff Tafel slopes, confirming the troublesome HER kinetics as expected. In the case of NMFP, the value of the Tafel slope was calculated as low as 77.65 $mV \cdot dec^{-1}$. By the result of the recent investigations, this result reveals that the NMFP has a close relationship with the alkaline Volmer-Heyrovsky mechanism, which the rate-determining step is electrochemical water dissociation with reactive hydrogen intermediate to

generate hydrogen molecule (H_2) [36]. Summarized HER performance of the prepared catalysts was shown in Figure 13c. Compared with several other catalysts represented in Table 3, NMFP exhibits eminent HER performance. In the way of assessing the durability of NMFP for use of stable and robust catalyst, 40 h of continuous CA test was initiated (Figure 13d). NMFP upheld the current density of 10 $mA \cdot cm^{-2}$ with an insignificant portion of degradation of performance.

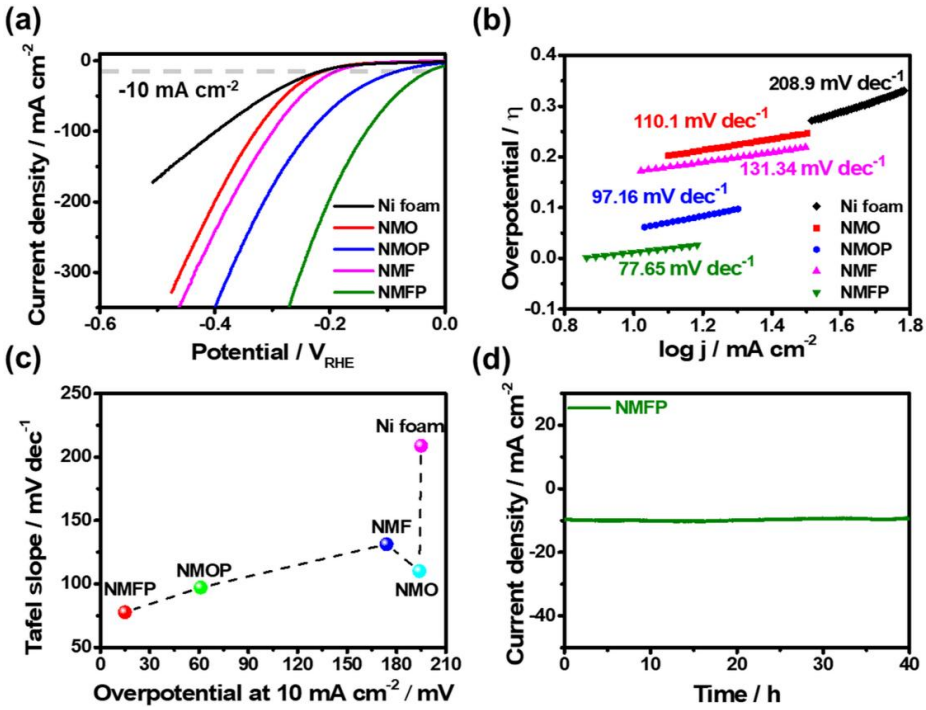

Figure 13. HER performance of NMFP and compared catalysts in 1.0 M KOH. LSV curves at room temperature (a) and the corresponding Tafel slopes (b). Summary of overpotential at current density of 10 mA·cm^{-2} and Tafel slope of the prepared catalysts (c). Time-dependent current density curve of NMFP at fixed overpotential of 15 mV (d).

Table 3. Comparison of the HER performance of NMFP with other reported electrocatalysts in 1.0 M KOH.

Materials	η at 10 mA cm^{-2} (mV vs. RHE)	Tafel slope (mA dec^{-1})	Substrate	Refs.
NMFP	15	77.6	NF	this work
NiCoP	32	37	NF	[1]
NixB/ f-MWCNT	116	70.4	GCE	[16]
N-NiCoP/NCF	78	83.17	NCF	[24]
O-$NiMoP_2$/Ni	31	62.11	NF	[25]
$Ni(OH)_2$-WP	77	71	CP	[36]
CP/CTs/Co-S	190	131	CP	[65]
CoS_2	193	88	CC	[66]
$NiCo_2S_4$ NW/NF	210	92.1	NF	[67]
NiFeSe@NiSe| O@CC	62	48.9	CC	[68]
NM-rods	118	65	NF	[69]

* GCE: glassy carbon electrode, NF: nickel foam, CC: carbon cloth, CP: carbon paper, NCF: Ni-Co foam

To further examine the catalytic performance of NMFP, the electrochemical OER test was accomplished. For comparison, NMO, NMOP, NMF, and Ni foam were also investigated in an identical environment. The LSV curves (Figure 14a) showed that NMFP required only 240 mV to reach a current density of 10 $mA \cdot cm^{-2}$. The other compared samples such as NMO (354 mV), NMOP (286 mV), NMF (320 mV), and Ni foam (453 mV) showed poorer catalytic ability than NMFP. The peak at around 1.40 V was known as a pre-OER oxidation peak of Ni-based material during the OER in 1.0 M alkaline media [59]. It is noteworthy that the oxidation peak shifts to higher potential after $K_3[Fe(CN)_6]$ treatment. This could be explained by the change in the oxidation state of Ni after the introduction of Fe [35]. It is widely known that the existence of Ni in a higher oxidation state is favorable for OER [60, 61]. To further investigate the OER kinetics of the prepared catalysts, the corresponding Tafel plots were suggested from the obtained LSV curves (Figure 14b), and later fitted to calculate the Tafel slope. The calculation implicated that NMFP owned the lowest slope value of 56.51 $mV \cdot dec^{-1}$, proposing the facile OER kinetics of the catalyst. Other compared samples such as NMO, NMOP, NMF, and Ni foam exhibited much higher Tafel slope of 105.21 $mV \cdot dec^{-1}$, 81.13 $mV \cdot dec^{-1}$, 93.86 $mV \cdot dec^{-1}$, and 171.76 $mV \cdot dec^{-1}$, respectively. OER performance of the prepared catalysts

was summarized in Figure 14c. Compared with several other reported catalysts (Table 4), NMFP shows competent OER performance. The integrity of NMFP as the promising OER catalyst, the evaluation of performance under 1.0 M KOH by long-term CA was conducted for over 40 h. As presented in Figure 14d., NMFP maintained its current density of 10 $mA \cdot cm^{-2}$ with a very small decay of initial performance.

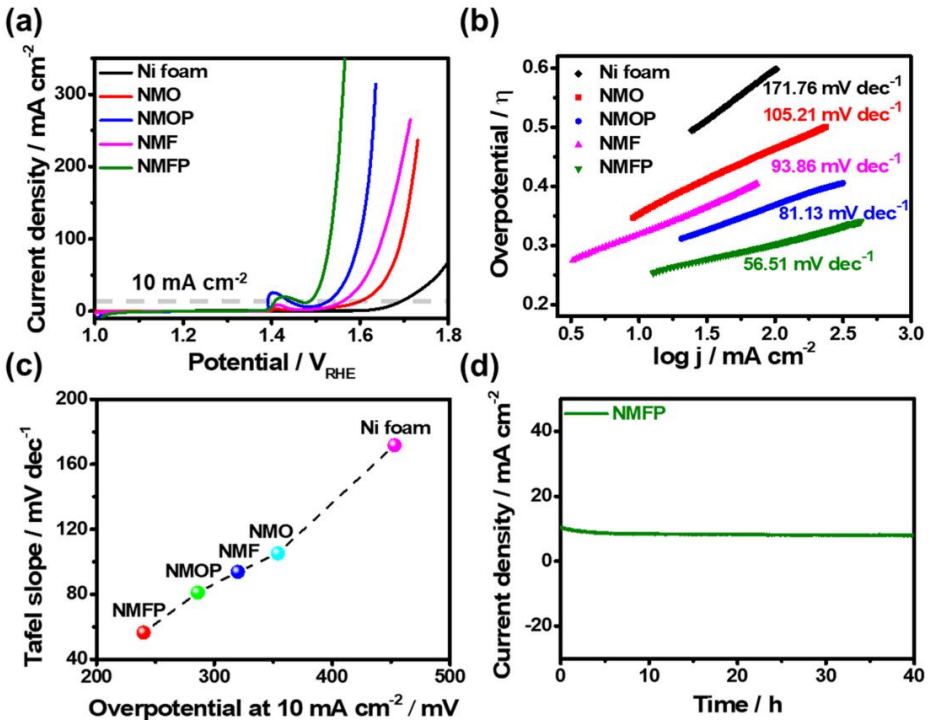

Figure 14. OER characteristics of the prepared catalysts in 1.0 M KOH. LSV curves at room temperature (a) and the corresponding Tafel slopes (b). Summary of overpotential at current density of 10 mA·cm^{-2} and Tafel slope of the prepared catalysts (c). Time-dependent current density curve of NMFP at fixed overpotential of 240 mV (d).

Table 4. Comparison of the OER performance of NMFP with other reported electrocatalysts in 1.0 M KOH.

Materials	η at 10 mA cm^{-2} (mV vs. RHE)	Tafel slope (mA dec^{-1})	Substrate	Refs.
NMFP	240	56.51	NF	this work
NiCoP	280	87	NF	[1]
NixB/ f-MWCNT	286	46.3	GCE	[16]
N-NiCoP/NCF	225	66.94	NCF	[24]
$Ni_{0.9}Fe_{0.1}MoO_4$	299	63	GCE	[35]
CP/CTs/Co-S	306	72	CP	[65]
CoS_2	276	81	CC	[66]
$NiCo_2S_4$ NW/NF	260	40.1	NF	[67]
NiFeSe@NiSe|O @CC	270	63.2	CC	[68]
$CoFe_2O_4$ NSs	275	42.1	GCE	[70]
NiCoS/$Ti_3C_2T_x$	365	58.2	GCE	[71]

* GCE: glassy carbon electrode, NF: nickel foam, CC: carbon cloth, CP: carbon paper, NCF: Ni-Co foam

For additional analysis, the electrochemical impedance spectroscopy (EIS) was investigated to examine the charge transfer resistance (R_{ct}) for both HER and OER (Figure 15). The measurement revealed that NMFP possesses the smallest R_{ct} of 2.78 Ω and 0.80 Ω for HER and OER, respectively among the investigated catalysts. An equivalent circuit model of this system and summarized information regarding the impedance spectroscopy is noted in Figure 16 and Table 5-6.

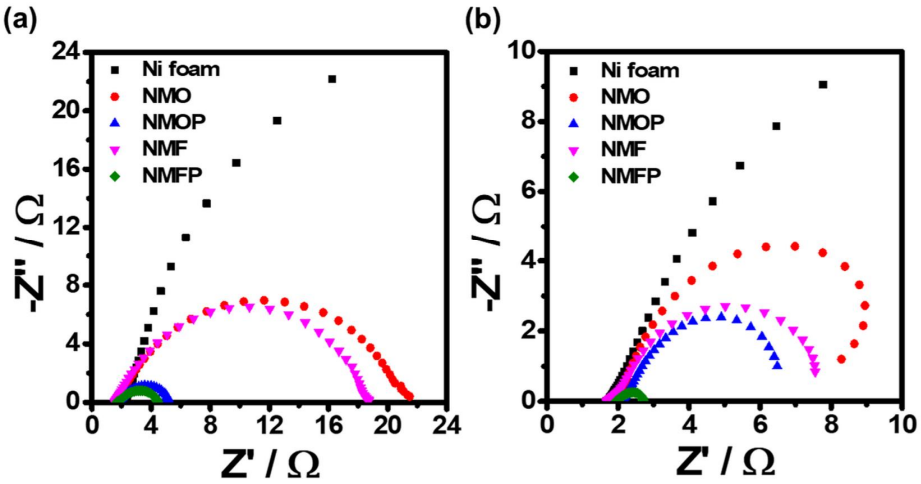

Figure 15. EIS spectra of the prepared catalysts for HER (a) and OER (b) in 1.0 M KOH. The EIS spectra of the catalysts was recorded with the frequency range from 10^{-2} to 10^{5} Hz at -0.1 V and 1.60 V for HER and OER, respectively.

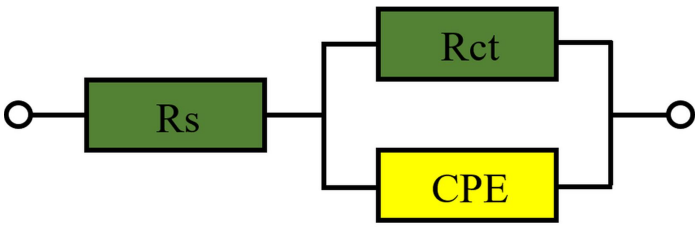

Figure 16. Randles circuit used for modeling of HER and OER kinetic processes. R_s is related to the solution resistance. R_{ct} is the charge transfer resistance of the catalyst/ electrolyte interface. CPE is the constant phase angle element, which is related to the double-layer capacitance of electrode under the catalytic process [64].

Table 5. Summary of each circuit parameters under the HER process.

Material	R_S (Ω)	CPE (F cm^{-2})		R_{ct} (Ω)
		Qy	Qa	
Ni foam	2.31	0.0005	0.917	59.9
NMO	1.68	0.004	0.768	19.8
NMOP	1.76	0.105	0.718	3.53
NMF	1.61	0.002	0.810	17.0
NMFP	1.74	0.108	0.654	2.78

Table 6. Summary of each circuit parameters under the OER process.

Material	R_S (Ω)	CPE (F cm^{-2})		R_{ct} (Ω)
		Qy	Qa	
Ni foam	1.77	0.023	0.877	26.5
NMO	1.91	0.439	1.049	7.65
NMOP	2.12	0.720	0.922	4.99
NMF	1.78	0.287	0.865	6.34
NMFP	1.95	0.775	0.694	0.80

The electrochemical active surface area (ECSA) of performed catalysts was also calculated through electrochemical double-layer capacitance (C_{dl}) measurement. The C_{dl} was calculated from the obtained CV with the scan rate of 20 $mV \cdot s^{-1}$ to 100 $mV \cdot s^{-1}$ at the potential window of 0.20 V to 0.30 V to avoid any faradaic current. Figure 17a-d indicates the obtained CV diagrams of NMO, NMOP, NMF, and NMFP. The calculated C_{dl} of NMFP exhibited 10.22 $mF \cdot cm^{-2}$, which was much higher than the other compared catalysts, indicating the larger exposed electrochemically active area (Figure 17e). The summarized result for C_{dl} is presented in Table 7.

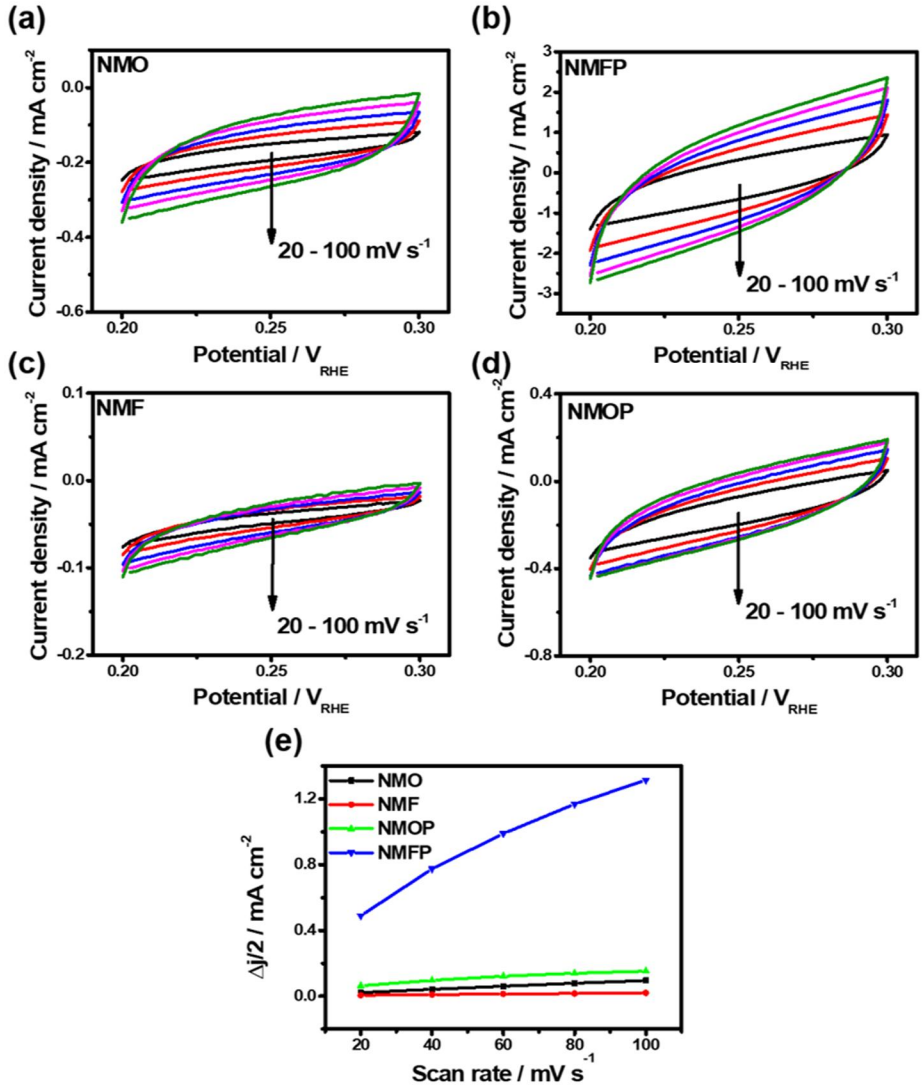

Figure 17. CV curves of NMO (a), NMOP (b), NMF (c), and NMFP (d) in 1.0 M KOH with different scan rates from 20 to 100 $mV \cdot s^{-1}$ (Potential range: 0.20- 0.30 V). Linear plots of differences in current density of NMO, NMOP, NMF, and NMFP (measured at 0.25 V) as a function of scan rate (e). From the (e), the double-layer capacitance can be calculated as follow: $C_{dl} = \Delta j / \upsilon$,

where $\Delta j = j_a - j_c$: charging current ($mA \cdot cm^{-2}$) at 0.25 V and υ : scan rate ($mV \cdot s^{-1}$).

Table 7. Summary of the calculated C_{dl} of NMFP and compared materials.

Material	C_{dl} ($mF\ cm^{-2}$)
NMO	0.918
NMOP	0.172
NMF	0.11
NMFP	10.22

To demonstrate NMFP as a sufficient catalyst to drive water splitting under alkaline medium, the conventional two-electrode test using NMFP on both the cathode and anode (denoted NMFP || NMFP) was conducted. For comparison, the commercial Pt/C and RuO_2 on Ni foam (denoted Pt/C || RuO_2) was prepared as HER and OER catalyst to benchmark the overall water splitting performance efficiency. As depicted in Figure 18a, the NMFP || NMFP could reach the current density of 100 $mA \cdot cm^{-2}$ by applying only 1.63 V, which is lower than compared Pt/C || RuO_2 (1.68 V) counterpart. Also, even the NMFP || NMFP was run over 3000 cycles (Figure 18b), the decay of performance was only 0.01 V to reach 100 $mA \cdot cm^{-2}$, which is significantly low compared to the initial catalysis operation. Similarly, the long-term durability test (Figure 18c) for water splitting using the NMFP || NMFP was initiated to check the integrity of the prepared catalyst. The prepared electrode maintained its original output of 10 $mA \cdot cm^{-2}$ as a water splitting catalyst for over 40 h without the huge drawback of performance.

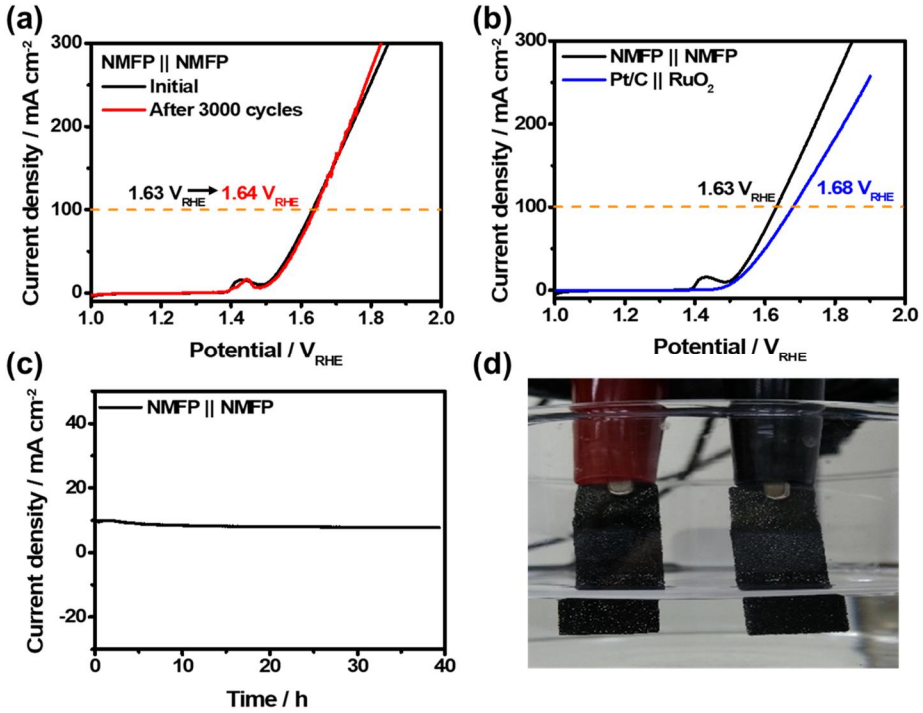

Figure 18. Overall water splitting performance of NMFP || NMFP in 1.0 M KOH. Comparison of polarization curves between NMFP || NMFP and Pt/C || RuO_2 (a). Polarization curves of NMFP || NMFP before and after 3000 cycles (b). Long-term stability test of NMFP || NMFP to maintain 10 mA·cm^{-2} for 40 h (c). Photograph image of NMFP || NMFP water electrolyzer (d).

After electrolysis for 40 h, the structural change of NMFP was investigated by SEM (Figure 19). As seen from Figure 19a-b, the morphology of NMFP was almost collapsed. This could be caused by long-term exposure to harsh alkaline media and vigorous generation of H_2 on the catalyst's surface. However, the nanorods was still tightly attached on the nickel foam. In the case of the anode (Figure 19c-d), the morphology of NMFP was relatively less damaged than that of the cathode. This phenomenon could be due to the slower generation of O_2 than that of H_2. Furthermore, the rod-like structure of NMFP was aggregated and changed into a web-like structure. The alteration in oxidation states of NMFP was further demonstrated by XPS (Figure 20). The peak positions of Ni $2p_{3/2}$ and $2p_{1/2}$ (Figure 20a) shifted towards higher binding energy, suggesting the change in oxidation state from 2^+ to 3^+ of the Ni during the catalytic process [27, 62]. For the P 2p spectra (Figure 20b), the P element peak was disappeared [62]. In the case of the O 1s spectra (Figure 20c), the P-O bond was diminished and the Ni-O bond was increased [63]. Meanwhile, the characteristic peaks for Fe and Mo elements were not observed (Figire 20d, e). These missing elements might be dissolved or covered by NiOOH amorphous layer during the long-term electrolysis. Also, the change in oxidation states of NMFP could be explained by the transition of -phosphate

into the –oxy(hydroxide) during the catalytic process [62].

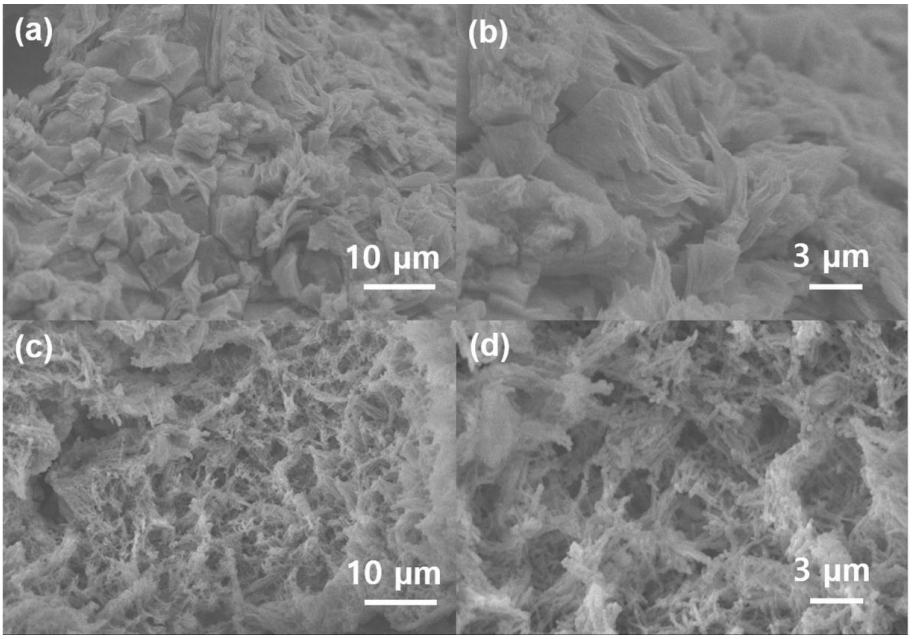

Figure 19. SEM images of NMFP after electrolysis for 40 h. NMFP at the cathode (a, b), NMFP at the anode (c, d).

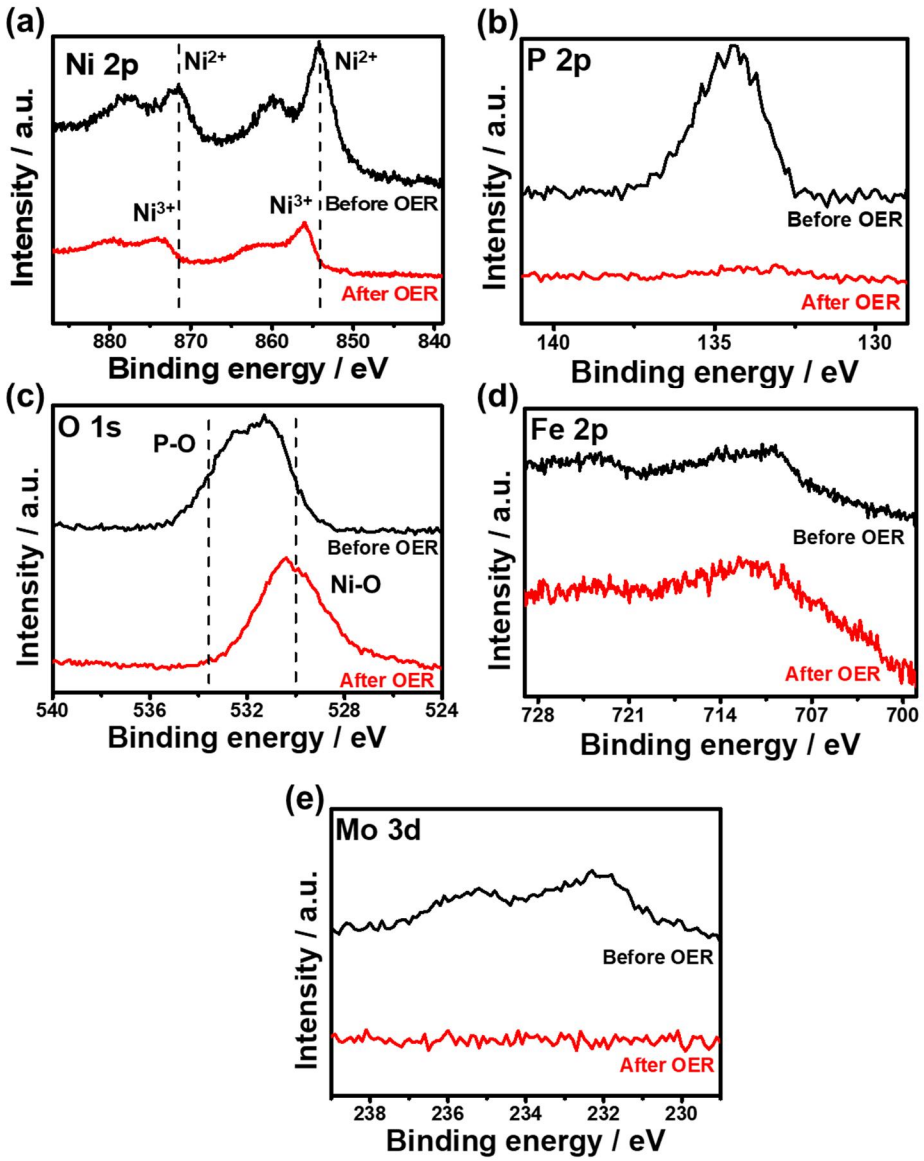

Figure 20. XPS analysis of NMFP at the anode after electrolysis. Ni 2p (a), P 2p (b), O 1s (c), Fe 2p (d), and Mo 3d (e).

4. Conclusion

In summary, the vertically-oriented Fe-Ni-Mo-P array on nickel foam (NMFP) was successfully synthesized through a template-assisted growth of PBA and phosphorization process. The prepared NMFP displayed competent catalytic performance for overall water splitting. To reach a current density of 10 $mA \cdot cm^{-2}$, the required overpotentials were 15 and 240 mV for HER and OER in 1.0 M KOH, respectively. The efficient catalytic kinetics were also verified by small Tafel slopes of 77.65 $mV \cdot dec^{-1}$ and 56.51 $mV \cdot dec^{-1}$ for HER and OER, respectively. In addition, the alkaline electrolyzer based on NMFP electrodes needed only 1.63 V to achieve a current density of 100 $mA \cdot cm^{-2}$ and showed little loss of catalytic performance after 3000 cycles. The remarkable catalytic performance of NMFP is attributed to (1) the well-ordered 1D structure upon a NF increases the electron transfer and ion accessibility; (2) the hybridization of Fe with NMO via forming the well-confined PBA not only enlarges catalytic surface area but also facilitates the charge transfer; (3) the post-phosphating modification further aids the overall water splitting efficiency. This work suggests a novel template-assisted method to obtain well-aligned PBA and their derivatives for overall water splitting catalysts. In addition, this apporach can be extended to a wide variety of studies based on nano-micro structured materials for energy

storage and conversion applications.

References

[1] H. Liang, A.N. Gandi, D.H. Anjum, X. Wang, U. Schwingenschlögl, H.N. Alshareef, Plasma-Assisted Synthesis of NiCoP for Efficient Overall Water Splitting, Nano Lett. 16 (2016) 7718–7725.

[2] A. Sivanantham, S. Shanmugam, Nickel selenide supported on nickel foam as an efficient and durable non-precious electrocatalyst for the alkaline water electrolysis, Appl. Catal. B Environ. 203 (2017) 485–493.

[3] S. Chu, Y. Cui, N. Liu, The path towards sustainable energy, Nat. Mater. 16 (2016) 16–22.

[4] Z. Qiu, C.W. Tai, G.A. Niklasson, T. Edvinsson, Direct observation of active catalyst surface phases and the effect of dynamic self-optimization in NiFe-layered double hydroxides for alkaline water splitting, Energy Environ. Sci. 12 (2019) 572–581.

[5] H. Wang, H.W. Lee, Y. Deng, Z. Lu, P.C. Hsu, Y. Liu, D. Lin, Y. Cui, Bifunctional non-noble metal oxide nanoparticle electrocatalysts through lithium-induced conversion for overall water splitting, Nat.

Commun. 6 (2015) 7261.

[6] N. Mahmood, Y. Yao, J.W. Zhang, L. Pan, X. Zhang, J.J. Zou, Electrocatalysts for Hydrogen Evolution in Alkaline Electrolytes: Mechanisms, Challenges, and Prospective Solutions, Adv. Sci. 5 (2018) 1700464.

[7] B. You, Y. Sun, Innovative Strategies for Electrocatalytic Water Splitting, Acc. Chem. Res. 51 (2018) 1571–1580.

[8] J. Deng, H. Li, S. Wang, D. Ding, M. Chen, C. Liu, Z. Tian, K.S. Novoselov, C. Ma, D. Deng, X. Bao, Multiscale structural and electronic control of molybdenum disulfide foam for highly efficient hydrogen production., Nat. Commun. 8 (2017) 14430.

[9] P. Chen, T. Zhou, M. Zhang, Y. Tong, C. Zhong, N. Zhang, L. Zhang, C. Wu, Y. Xie, 3D Nitrogen-Anion-Decorated Nickel Sulfides for Highly Efficient Overall Water Splitting, Adv. Mater. 29 (2017) 1701584.

[10] F. Song, X. Hu, Exfoliation of layered double hydroxides for enhanced oxygen evolution catalysis, Nat. Commun. 5 (2014) 4477.

[11] M. Zeng, Y. Li, Recent advances in heterogeneous electrocatalysts for

the hydrogen evolution reaction, J. Mater. Chem. A. 3 (2015) 14942–14962.

[12] R. Zhang, X. Wang, S. Yu, T. Wen, X. Zhu, F. Yang, X. Sun, X. Wang, W. Hu, Ternary $NiCo_2P_x$ Nanowires as pH-Universal Electrocatalysts for Highly Efficient Hydrogen Evolution Reaction, Adv. Mater. 29 (2017) 1605502.

[13] N.-T. Suen, S.-F. Hung, Q. Quan, N. Zhang, Y.-J. Xu, H.M. Chen, Electrocatalysis for the oxygen evolution reaction: recent development and future perspectives., Chem. Soc. Rev. 46 (2017) 337–365.

[14] S. Cherevko, S. Geiger, O. Kasian, N. Kulyk, J.-P. Grote, A. Savan, B.R. Shrestha, S. Merzlikin, B. Breitbach, A. Ludwig, K.J.J.J. Mayrhofer, Oxygen and hydrogen evolution reactions on Ru, RuO_2, Ir, and IrO_2 thin film electrodes in acidic and alkaline electrolytes: A comparative study on activity and stability, Catal. Today. 262 (2016) 170–180.

[15] Y. Li, H. Zhang, M. Jiang, Y. Kuang, X. Sun, X. Duan, Ternary NiCoP nanosheet arrays: An excellent bifunctional catalyst for alkaline overall water splitting, Nano Res. 9 (2016) 2251–2259.

[16] X. Chen, Z. Yu, L. Wei, Z. Zhou, S. Zhai, J. Chen, Y. Wang, Q. Huang, H. Enis Karahan, X. Liao, Y. Chen, Ultrathin nickel boride nanosheets anchored on functionalized carbon nanotubes as bifunctional electrocatalysts for overall water splitting, J. Mater. Chem. A. 7 (2019) 764–774.

[17] J. Xing, H. Li, M. Ming-Cheng Cheng, S.M. Geyer, K.Y.S. Ng, Electro-synthesis of 3D porous hierarchical Ni-Fe phosphate film/Ni foam as a high-efficiency bifunctional electrocatalyst for overall water splitting, J. Mater. Chem. A. 4 (2016) 13866–13873.

[18] Y. Pan, K. Sun, S. Liu, X. Cao, K. Wu, W.C. Cheong, Z. Chen, Y. Wang, Y. Li, Y. Liu, D. Wang, Q. Peng, C. Chen, Y. Li, Core-Shell ZIF-8@ZIF-67-Derived CoP Nanoparticle-Embedded N-Doped Carbon Nanotube Hollow Polyhedron for Efficient Overall Water Splitting, J. Am. Chem. Soc. 140 (2018) 2610–2618.

[19] G. Zhang, G. Wang, Y. Liu, H. Liu, J. Qu, J. Li, Highly Active and Stable Catalysts of Phytic Acid-Derivative Transition Metal Phosphides for Full Water Splitting, J. Am. Chem. Soc. 138 (2016) 14686–14693.

[20] J. Yu, Q. Li, Y. Li, C.Y. Xu, L. Zhen, V.P. Dravid, J. Wu, Ternary Metal Phosphide with Triple-Layered Structure as a Low-Cost and Efficient Electrocatalyst for Bifunctional Water Splitting, Adv. Funct. Mater. 26 (2016) 7644–7651.

[21] J. Joo, T. Kim, J. Lee, S. Il Choi, K. Lee, Morphology-Controlled Metal Sulfides and Phosphides for Electrochemical Water Splitting, Adv. Mater. 31 (2019) 186682.

[22] S. Jin, Are Metal Chalcogenides, Nitrides, and Phosphides Oxygen Evolution Catalysts or Bifunctional Catalysts?, ACS Energy Lett. 2 (2017) 1937–1938.

[23] C. Du, L. Yang, F. Yang, G. Cheng, W. Luo, Nest-like NiCoP for Highly Efficient Overall Water Splitting, ACS Catal. 7 (2017) 4131–4137.

[24] C. Tang, L. Gan, R. Zhang, W. Lu, X. Jiang, A.M. Asiri, X. Sun, J. Wang, L. Chen, Ternary $Fe_xCo_{1-x}P$ Nanowire Array as a Robust Hydrogen Evolution Reaction Electrocatalyst with Pt-like Activity: Experimental and Theoretical Insight, Nano Lett. 16 (2016) 6617–6621.

[25] L. Zhang, X. Wang, X. Zheng, L. Peng, J. Shen, R. Xiang, Z. Deng, L. Li, H. Chen, Z. Wei, Oxygen-Incorporated $NiMoP_2$ Nanowire Arrays for Enhanced Hydrogen Evolution Activity in Alkaline Solution , ACS Appl. Energy Mater. 1 (2018) 5482-5489.

[26] W. Hua, H. Liu, J.-G. Wang, B. Wei, Self-Supported $Ni(P, O)_x$·MoO_x Nanowire Array on Nickel Foam as an Efficient and Durable Electrocatalyst for Alkaline Hydrogen Evolution, Nanomaterials. 7 (2017) 433.

[27] K.Li, J. Ma, X. Guan, H.He, M. Wang, G. Zhang, F. Zhang, X. Fan, W. Peng, Y. Li, 3D self-supported $Ni(PO_3)_2$-MoO_3 nanorods anchored on nickel foam for highly efficeint overall water splitting, Nanoscale. 10 (2018) 22173-22179.

[28] W. Xi, G. Yan, H. Tan, L. Xiao, S. Cheng, S.U. Khan, Y. Wang, Y. Li, Superaerophobic P-doped $Ni(OH)_2$/$NiMoO_4$ hierarchical nanosheet arrays grown on Ni foam for electrocatalytic overall water splitting, Dalt. Trans. 47 (2018) 8787–8793.

[29] H. Xu, J. Wei, K. Zhang, Y. Shiraishi, Y. Du, Hierarchical NiMo Phosphide Nanosheets Strongly Anchored on Carbon Nanotubes as

Robust Electrocatalysts for Overall Water Splitting, ACS Appl. Mater. Interfaces. 10 (2018) 29647–29655.

[30] J.R. McKone, B.F. Sadtler, C.A. Werlang, N.S. Lewis, H.B. Gray, Ni-Mo nanopowders for efficient electrochemical hydrogen evolution, ACS Catal. 3 (2013) 166–169.

[31] J. Zhang, T. Wang, P. Liu, Z. Liao, S. Liu, X. Zhuang, M. Chen, E. Zschech, X. Feng, Efficient hydrogen production on $MoNi_4$ electrocatalysts with fast water dissociation kinetics, Nat. Commun. 8 (2017) 15437.

[32] K. Hu, M. Wu, S. Hinokuma, T. Ohto, M. Wakisaka, J.I. Fujita, Y. Ito, Boosting electrochemical water splitting: via ternary NiMoCo hybrid nanowire arrays, J. Mater. Chem. A. 7 (2019) 2156–2164.

[33] J. Zhao, X. Ren, H. Ma, X. Sun, Y. Zhang, T. Yan, Q. Wei, D. Wu, Synthesis of Self-Supported Amorphous $CoMoO_4$ Nanowire Array for Highly Efficient Hydrogen Evolution Reaction, ACS Sustain. Chem. Eng. 5 (2017) 10093–10098.

[34] X. Zhao, H. Ren, L. Luo, Gas Bubbles in Electrochemical Gas Evolution Reactions, Langmuir. 35(2019) 5392-5408.

[35] J. Chen, G. Zhao, Y. Chen, K. Rui, H. Mao, S.X. Dou, W. Sun, Iron-Doped Nickel Molybdate with Enhanced Oxygen Evolution Kinetics, Chem. Eur. J. 25 (2019) 280–284.

[36] D. Kim, J. Park, J. Lee, Z. Zhang, K. Yong, $Ni(OH)_2$ -WP Hybrid Nanorod Arrays for Highly Efficient and Durable Hydrogen Evolution Reactions in Alkaline Media, ChemSusChem. 11 (2018) 3618–3624.

[37] Y. Li, H. Xu, H. Huang, C. Wang, L. Gao, T. Ma, One-dimensional MoO_2 -$Co_2Mo_3O_8$ @C nanorods: a novel and highly efficient oxygen evolution reaction catalyst derived from metal-organic framework composites, Chem. Commun. 54 (2018) 2739–2742.

[38] X. Guo, X. Yu, Z. Feng, J. Liang, Q. Li, Z. Lv, B. Liu, C. Hao, G. Li, Intercalation Synthesis of Prussian Blue Analogue Nanocone and Their Conversion into Fe-Doped Co_xP Nanocone for Enhanced Hydrogen Evolution, ACS Sustain. Chem. Eng. 6 (2018) 8150–8158.

[39] N. Yang, C. Tang, K. Wang, G. Du, A.M. Asiri, X. Sun, Iron-doped nickel disulfide nanoarray: A highly efficient and stable electrocatalyst for water splitting, Nano Res. 9 (2016) 3346–3354.

[40] Y. Ge, P. Dong, S.R. Craig, P.M. Ajayan, M. Ye, J. Shen,

Transforming Nickel Hydroxide into 3D Prussian Blue Analogue Array to Obtain Ni_2P/Fe_2P for Efficient Hydrogen Evolution Reaction, Adv. Energy Mater. 8 (2018) 1800484.

[41] Y. Wang, J. Ma, J. Wang, S. Chen, H. Wang, J. Zhang, Interfacial Scaffolding Preparation of Hierarchical PBA-Based Derivative Electrocatalysts for Efficient Water Splitting, Adv. Energy Mater. 9 (2019) 1802939.

[42] L.M. Cao, Y.W. Hu, D.C. Zhong, T.B. Lu, Template-Directed Growth of Bimetallic Prussian Blue-Analogue Nanosheet Arrays and Their Derived Porous Metal Oxides for Oxygen Evolution Reaction, ChemSusChem. 11 (2018) 3708–3713.

[43] H. Yan, Y. Xie, A. Wu, Z. Cai, L. Wang, C. Tian, X. Zhang, H. Fu, Anion-Modulated HER and OER Activities of 3D Ni–V-Based Interstitial Compound Heterojunctions for High-Efficiency and Stable Overall Water Splitting, Adv. Mater. 1901174 (2019) 1901174.

[44] M. Song, Z. Zhang, Q. Li, W. Jin, Z. Wu, G. Fu, X. Liu, Ni-foam supported Co(OH)F and Co-P nanoarrays for energy-efficient hydrogen production via urea electrolysis, J. Mater. Chem. A. 7 (2019)

3697–3703.

[45] Y. Li, C. Zhao, Enhancing Water Oxidation Catalysis on a Synergistic Phosphorylated NiFe Hydroxide by Adjusting Catalyst Wettability, ACS Catal. 7 (2017) 2535–2541.

[46] K.J.H. Lim, G. Yilmaz, Y.F. Lim, G.W. Ho, Multi-compositional hierarchical nanostructured Ni_3S_2@MoS_x/NiO electrodes for enhanced electrocatalytic hydrogen generation and energy storage, J. Mater. Chem. A. 6 (2018) 20491–20499.

[47] Y. Xu, H. Xuan, J. Gao, T. Liang, X. Han, J. Yang, Y. Zhang, H. Li, P. Han, Y. Du, Hierarchical three-dimensional $NiMoO_4$-anchored rGO/Ni foam as advanced electrode material with improved supercapacitor performance, J. Mater. Sci. 53 (2018) 8483–8498.

[48] D. Yang, L. Yang, L. Zhong, X. Yu, L. Feng, Urea electro-oxidation efficiently catalyzed by nickel-molybdenum oxide nanorods, Electrochim. Acta. 295 (2019) 524–531.

[49] C. Qing, Y. Liu, X. Sun, X. Ouyang, H. Wang, D. Sun, B. Wang, Q. Zhou, L. Xu, Y. Tang, Controlled growth of $NiMoO_4 \cdot H_2O$ nanoflake and nanowire arrays on Ni foam for superior performance of

asymmetric supercapacitors, RSC Adv. 6 (2016) 67785–67793.

[50] M.C. Liu, L. Kang, L. Bin Kong, C. Lu, X.J. Ma, X.M. Li, Y.C. Luo, Facile synthesis of $NiMoO_4 \cdot xH_2O$ nanorods as a positive electrode material for supercapacitors, RSC Adv. 3 (2013) 6472–6478.

[51] X. Zhang, P. Liu, Y. Sun, T. Zhan, Q. Liu, L. Tang, J. Guo, Y. Xia, $Ni_3[Fe(CN)_6]_2$ nanocubes boost the catalytic activity of Pt for electrochemical hydrogen evolution, Inorg. Chem. Front. 5 (2018) 1683–1689.

[52] Y. Feng, H.S. Han, K.M. Kim, S. Dutta, T. Song, Self-templated Prussian blue analogue for efficient and robust electrochemical water oxidation, J. Catal. 369 (2019) 168–174.

[53] S. Lei, Q.H. Li, Y. Kang, Z.G. Gu, J. Zhang, Epitaxial growth of oriented prussian blue analogue derived well-aligned $CoFe_2O_4$ thin film for efficient oxygen evolution reaction, Appl. Catal. B Environ. 245 (2019) 1–9.

[54] Z. Lei, J. Bai, Y. Li, Z. Wang, C. Zhao, Fabrication of Nanoporous Nickel-Iron Hydroxylphosphate Composite as Bifunctional and Reversible Catalyst for Highly Efficient Intermittent Water Splitting,

ACS Appl. Mater. Interfaces. 9 (2017) 35837–35846.

[55] Q. Chen, R. Wang, F. Lu, X. Kuang, Y. Tong, X. Lu, Boosting the Oxygen Evolution Reaction Activity of $NiFe_2O_4$ Nanosheets by Phosphate Ion Functionalization, ACS Omega. 4 (2019) 3493–3499.

[56] F. Qin, Z. Zhao, M.K. Alam, Y. Ni, F. R. Hernandez, L. Yu, S. Chen, Z. Ren, Z. Wang, J. Bao, Trimetallic NiFeMo for Overall Electrochemical Water Splitting with a Low Cell Voltage, ACS Energy Lett. 3 (2018) 546–554.

[57] Q. Zhang, Y. Deng, Z. Hu, Y. Liu, M. Yao, P. Liu, Seaurchin-like hierarchical $NiCo_2O_4$@$NiMoO_4$ core-shell nanomaterials for high performance supercapacitors, Phys. Chem. Chem. Phys. 16 (2014) 23451–23460.

[58] J. Zhang, W. Wu, C. Zhang, Z. Ren, X. Qian, Prussian-blue analog-derived Co_3S_4/MoS_2 porous nanocubes as enhanced Pt-free electrode catalysts for high-efficiency dye-sensitized solar cells, Appl. Surf. Sci. 484 (2019) 1111–1117.

[59] M. Liu, W. Zheng, S. Ran, S.T. Boles, L.Y.S. Lee, Overall Water-Splitting Electrocatalysts Based on 2D CoNi-Metal-Organic

Frameworks and Its Derivative, Adv. Mater. Interfaces. 5 (2018) 1800849.

[60] C.X. Guo, C.M. Li, Room temperature-formed iron-doped nickel hydroxide on nickel foam as a 3D electrode for low polarized and high-current-density oxygen evolution, Chem. Commun. 54 (2018) 3262–3265.

[61] D. Zhu, J. Liu, L. Wang, Y. Du, Y. Zheng, K. Davey, S.Z. Qiao, A 2D metal-organic framework/$Ni(OH)_2$ heterostructure for an enhanced oxygen evolution reaction, Nanoscale. 11 (2019) 3599–3605

[62] P. Wang, Z. Pu, Y. Li, L. Wu, Z. Tu, M. Jiang, Z. Kou, I.S. Amiinu, S. Mu, Iron-Doped Nickel Phosphide Nanosheet Arrays: An Efficient Bifunctional Electrocatalyst for Water Splitting, ACS Appl. Mater. Interfaces. 9 (2017) 26001–26007.

[63] H. Yang, S. Luo, Y. Bao, Y. Luo, J. Jin, J. Ma, In situ growth of ultrathin Ni-Fe LDH nanosheets for high performance oxygen evolution reaction, Inorg. Chem. Front. 4 (2017) 1173–1181.

[64] Q. Zhang, T. Li, J. Liang, N. Wang, X. Kong, J. Wang, H. Qian, Y. Zhou, F. Liu, C. Wei, Y. Zhao, X. Zhang, Highly wettable and metallic

NiFe-phosphate/phosphide catalyst synthesized by plasma for highly efficient oxygen evolution reaction, J. Mater. Chem. A. 6 (2018) 7509–7516.

[65] J. Wang, H.X. Zhong, Z.L. Wang, F.L. Meng, X.B. Zhang, Integrated Three-Dimensional Carbon Paper/Carbon Tubes/Cobalt-Sulfide Sheets as an Efficient Electrode for Overall Water Splitting, ACS Nano. 10 (2016) 2342–2348.

[66] C. Guan, X. Liu, A.M. Elshahawy, H. Zhang, H. Wu, S.J. Pennycook, J. Wang, Metal-organic framework derived hollow CoS_2 nanotube arrays: an efficient bifunctional electrocatalyst for overall water splitting, Nanoscale Horizons. 2 (2017) 342–348.

[67] A. Sivanantham, P. Ganesan, S. Shanmugam, Hierarchical $NiCo_2S_4$ Nanowire Arrays Supported on Ni Foam: An Efficient and Durable Bifunctional Electrocatalyst for Oxygen and Hydrogen Evolution Reactions, Adv. Funct. Mater. 26 (2016) 4661–4672.

[68] M. Lang, E. Delahaye, D. Foix, D. Ihiawakrim, O. Ersen, C. Leuvrey, J.M. Grenèche, G. Rogez, P. Rabu, Pseudomorphic Transformation of Layered Simple Hydroxides into Prussian Blue Analogue Nanoplatelets, Eur. J. Inorg. Chem. 2016 (2016) 2030–2038.

[69] K.J.H. Lim, G. Yilmaz, Y.F. Lim, G.W. Ho, Multi-compositional hierarchical nanostructured Ni_3S_2@MoS_x/NiO electrodes for enhanced electrocatalytic hydrogen generation and energy storage, J. Mater. Chem. A. 6 (2018) 20491–20499.

[70] H. Fang, T. Huang, D. Liang, M. Qiu, Y. Sun, S. Yao, J. Yu, M.M. Dinesh, Z. Guo, Y. Xia, S. Mao, Prussian blue analog-derived 2D ultrathin $CoFe_2O_4$ nanosheets as high-activity electrocatalysts for the oxygen evolution reaction in alkaline and neutral media, J. Mater. Chem. A. 7 (2019) 7328–7332.

[71] H. Zou, B. He, P. Kuang, J. Yu, K. Fan, Metal-Organic Framework-Derived Nickel-Cobalt Sulfide on Ultrathin Mxene Nanosheets for Electrocatalytic Oxygen Evolution, ACS Appl. Mater. Interfaces. 10 (2018) 22311–22319.

국 문 초 록

수전해를 통한 수소 및 산소발생 기술은 화석연료의 고갈 및 화석연료 사용에 따른 환경오염문제를 해결 할 수 있는 기술 중 하나로 각광받고 있다. 열역학적으로 수전해에 필요한 에너지는 1.23 V이다. 하지만 산소 및 수소발생 반응의 복잡한 반응경로 및 반응생성물로 인해 실제로 1.23 V이상의 전압이 필요하고, 이를 과전압이라 한다. 현재 반응에 필요한 과전압을 낮추기 위해 산업적으로 사용되는 촉매는 Pt 및 RuO_2, IrO_2 과 같은 귀금속 기반의 촉매물질이다. 하지만 이들은 매장량이 적어 가격 경쟁력이 떨어지고, 낮은 내구성 문제로 대량화에 어려움이 있다. 따라서 귀금속 촉매를 대체할 수 있는 새로운 물질을 개발하는 것이 필요하다. 본 연구는 Fe가 포함된 Ni-Mo-P 어레이를 니켈 폼위에 성장 (NMFP) 시키는 방법을 제시하고, 이 물질이 효율적인 수전해 촉매로 사용될 수 있음을 증명하였다. NMFP는 수열합성법을 통해 $NiMoO_4 \cdot xH_2O$를 니켈 폼위에 성장시킨 후 (NMO), 표면에 니켈-철 프루시안 블루 아날로그 (Ni-Fe PBA)를 합성한 뒤, 인 도핑을 통해 합성 할 수 있다. 합성 과정에서 NMO는 PBA가 잘 분리되어 성장할 수 있도록 돕는 템플릿 및 Ni 이온 제공원으로서 작용하고, $K_3[Fe(CN)_6$ 는 Ni-Fe PBA의 Fe 이온 및 유기 링커로 작용한다.

합성된 NMFP는 Fe 첨가 효과 및 많은 활성점이 노출 되어 있는 정렬된 나노로드 구조로 인해 알칼라인 전해질 (1.0 M KOH)에서 우수한 HER, OER 성능을 나타냈으며, 40시간 반응 후에도 성능 저하를 거의 보이지 않았다. NMFP를 양극, 음극으로 사용한 셀은 100 $mA \cdot cm^{-2}$ 가 회로에 흐르기 위해 1.63 V (과전압 400 mV)의 전압이 필요하고, 3000 사이클 사용 후에도 우수한 성능을 나타냈다.

주요어: 수전해, 산화니켈몰리브데넘, 템플릿 합성법, 금속 인화물

학 번: 2017-20540